scientific reports

Check for updates

OPEN

Dapagliflozin inhibits ferroptosis and ameliorates renal fibrosis in diabetic C57BL/6J mice

Zhen Zhang[1,2,3,6], Luxin Li[2,4]✉, Yucen Dai[2,4,6], Yifei Lian[3,6], Haixu Song[5], Xin Dai[3], Ranyu Su[4], Jiaxing Yin[5] & Ruimin Gu[1]✉

Diabetic nephropathy (DN) is a common complication of diabetes and a major cause of end-stage renal disease, with complex pathogenesis involving inflammation, oxidative stress, fibrosis, and ferroptosis. Ferroptosis is linked to DN progression, yet treatment options are limited, particularly for targeting ferroptosis. Dapagliflozin (DAPA), an SGLT2 inhibitor, shows renal protective effects in diabetes, but its role in renal fibrosis and ferroptosis in DN is unclear. This study investigated DAPA's effect on renal fibrosis in DN by inhibiting ferroptosis, using a streptozotocin-induced diabetic mouse model. Results indicated that DAPA improved renal function, reduced fibrosis, and suppressed ferroptosis markers in diabetic mice. In vitro, DAPA inhibited ferroptosis and fibrosis in HK-2 cells under high glucose conditions. Molecular docking and network pharmacology suggested DAPA's anti-fibrotic and anti-ferroptotic effects may involve the Nrf2 and TGF-β signaling pathways. DAPA also reduced serum creatinine and blood urea nitrogen in diabetic mice, improved glomerulosclerosis and interstitial fibrosis, decreased iron deposition, and enhanced antioxidant activity. Overall, DAPA's multi-target mechanisms significantly improve DN progression, suggesting its potential as a targeted therapy against ferroptosis. Future studies should further explore DAPA's applications.

Keywords Dapagliflozin, Diabetic nephropathy, Renal fibrosis, TGF-β/Smad pathway, Ferroptosis

Abbreviations

ACSL4	Acyl-CoA synthetase long-chain family 4
BP	Biological process
BUN	Blood urea nitrogen
CASP3	Caspase-3
CAT	Catalase
CC	Cellular component
Col1	Type I collagen
Col3	Type III collagen
COX2	Cyclooxygenase 2
DAPA	Dapagliflozin
DM	Diabetes mellitus
DN	Diabetic nephropathy
EMT	Epithelial-mesenchymal transition
EndoMT	Endothelial-to-mesenchymal transition
ESR1	Estrogen receptor 1
FN	Fibronectin
FTH1	Ferritin heavy chain 1
GO	Gene Ontology
GPX4	Glutathion peroxidase 4
GSH	Glutathione
HE	Hematoxylin and eosin

[1]College of Pharmacy, Harbin Medical University, Harbin 150000, Harbin, China. [2]Heilongjiang Key Laboratory of Tissue Damage and Repair, Mudanjiang Medical University, Mudanjiang 157000, Heilongjiang, China. [3]School of First Clinical Medical College, Mudanjiang Medical University, Mudanjiang 157000, China. [4]College of Life Sciences, Mudanjiang Medical University, Mudanjiang 157000, China. [5]Affiliated Hongqi Hospital, Mudanjiang Medical University, Mudanjiang 157000, China. [6] Zhen Zhang, Yucen Dai, and Yifei Lian contributed equally to this work. ✉email: liluxin@mdjmu.edu.cn; ruimingu2916@163.com

IL-6	Interleukin-6
KEGG	Kyoto Encyclopedia of Genes and Genomes
LDH	Lactate dehydrogenase
MCC	Maximum clique centrality
MDA	Malondialdehyde
MF	Molecular function
MTOR	Mammalian target of rapamycin
NFE2L2	Nuclear factor erythroid 2-related factor 2
NFκB	Nuclear factor kappa-B
NOX1	NADPH oxidase 1
NOX4	NADPH oxidase 4
PAS	Periodic acid-Schiff
PTSG2	Prostaglandin-endoperoxide synthase 2
qRT-PCR	Quantitative Real-Time PCR
RELA	Rela proto-oncogene
RF	Renal fibrosis
ROS	Reactive oxygen species
Scr	Serum creatinine
SGLT2	Sodium-dependent glucose transporters 2
SOD	Superoxide dismutase
SRC	Src proto-oncogene
STAT3	Signal transducer and activator of transcription 3
STZ	Streptozotocin
TGF-β	Transforming growth factor-β
TNF	Tumor necrosis factor
TP53	Tumor protein 53
Vdmin	End-diastolic velocity
Vsmax	Peak systolic velocity
α-SMA	Alpha-smooth muscle actin

Diabetes mellitus (DM) is classified as one of the fastest-growing diseases globally, with projected figures suggesting it will affect 693 million adults by 2045[1]. Diabetic nephropathy (DN) constitutes a prevalent and significant chronic complication emanating from DM, and it stands as the leading cause of end-stage renal disease. The pathogenesis of DN is intricate, encompassing elements such as inflammation, oxidative stress, glucolipid metabolic disturbances, and fibrosis[2,3]. Numerous studies have confirmed that renal fibrosis (RF) is a pivotal factor in the progressive deterioration of DN[4,5].

The TGF-β/Smad signaling pathway plays a crucial role in the development of fibrosis, especially in RF related to DN[6]. Transforming growth factor-β (TGF-β) serves as a key mediator in RF, facilitating this process through the activation of downstream signaling pathways, which leads to epithelial-mesenchymal transition (EMT), endothelial-to-mesenchymal transition (EndoMT), and the activation of myofibroblasts[7,8]. Given that the unregulated activation of the TGF-β/Smad signaling pathway in RF directly contributes to the exacerbation of DN[9,10]. Therefore, the pursuit of novel therapeutic drugs or strategies to curtail RF is of utmost importance for ameliorating the progression of DN.

Recent research has concentrated on the mechanisms underpinning the relationship between inflammation and fibrosis in promoting tubular cell death[11,12]. Ferroptosis, a recently identified form of iron-dependent cell demise characterized by the accumulation of intracellular lipid peroxides, has received extensive research[13]. Numerous studies have confirmed a close association between the development of DN and ferroptosis[14,15]. Consequently, regulating ferroptosis to alleviate RF presents a potential target for clinical treatment, thereby facilitating the integration of scientific research with clinical practice and establishing a foundation for the development of drugs that specifically and effectively regulate ferroptosis to treat DN.

DAPA is an effective antihyperglycemic drug that has been applied in clinical practice in recent years and belongs to the class of sodium-dependent glucose transporters 2 (SGLT2) inhibitors[16]. SGLTs are integral transmembrane proteins that utilize the sodium gradient established by the sodium-potassium pump to co-transport sodium and glucose into cells[17]. Notably, SGLT2 predominantly mediates renal glucose reabsorption, accounting for approximately 90% of total glucose reabsorption into the bloodstream. DAPA functions by inhibiting this protein, which subsequently reduces glucose reabsorption and lowers blood glucose levels[18]. Research has demonstrated that DAPA can exert hypoglycemic effects independently of insulin levels and may also provide protective benefits to the kidneys[19,20]. Furthermore, some researchers have investigated the potential of DAPA in targeting ferroptosis in kidney-related diseases[21–23]. Although these studies suggest that ferroptosis participates in the renal tubular protective effects of DAPA in diabetes, the exact mechanisms governing this regulatory process remain elusive and require further exploration.

Recently, the convergence of network pharmacology and molecular docking has emerged as a prominent research focus, dedicated to elucidating the intricate relationships between drugs and diseases[24]. In this setting, the current study utilizes in vivo and in vitro experiments in combination with network pharmacology and molecular docking to analyze the impacts and underlying mechanisms of DAPA on ferroptosis related to diabetic RF. The comprehensive workflow of the experiments is depicted in Fig. 1.

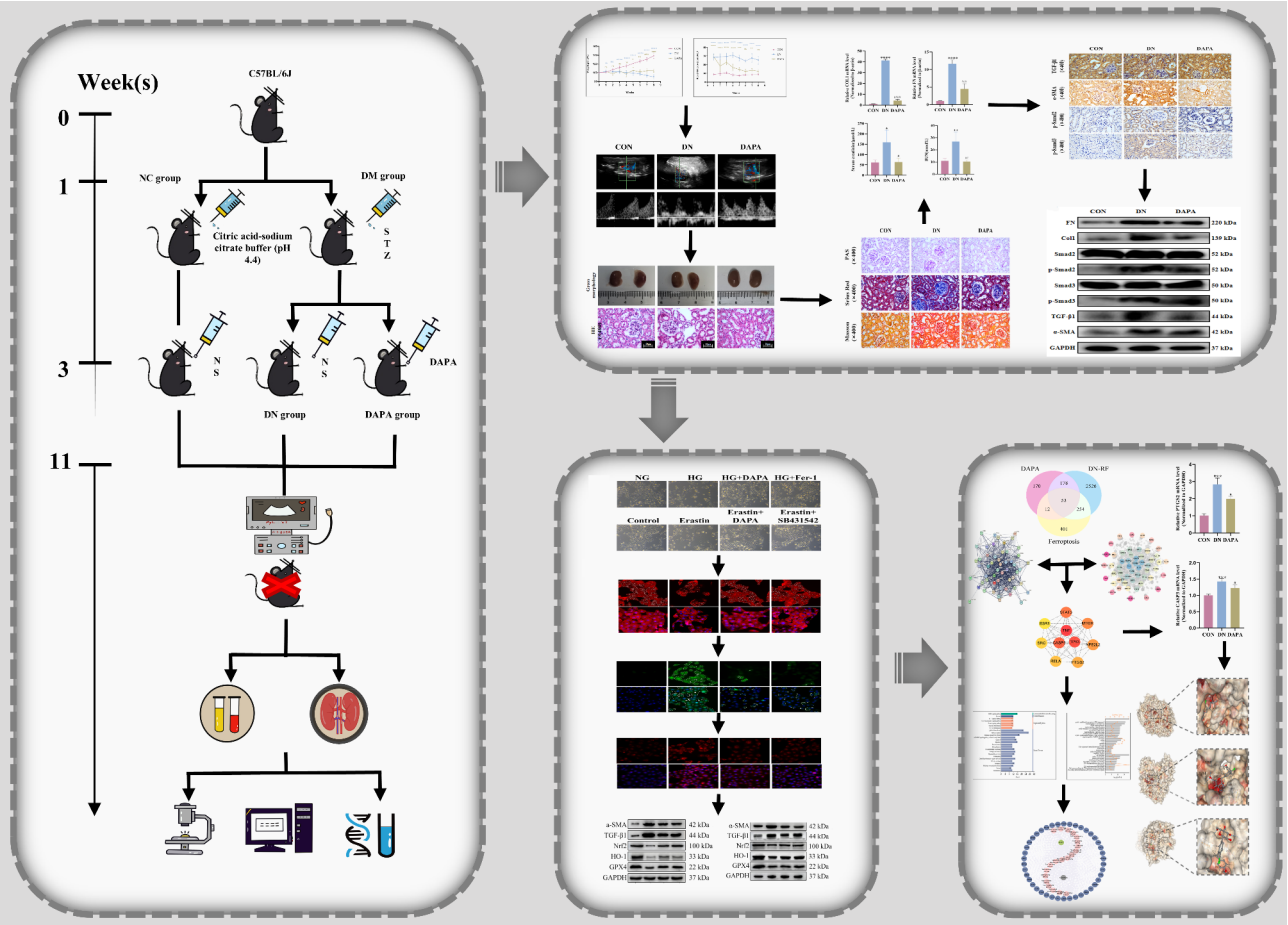

Fig. 1. Flow chart of this study.

Results

Effect of DAPA on physiological indices, renal pathological morphology, and renal function in mice

C57BL/6J mice were employed in this study. Diabetic mouse models were swiftly induced through intraperitoneal injection of streptozotocin (STZ), leading to pancreatic islet dysfunction within approximately five days. Following the establishment of the model, the treatment group received DAPA via gavage for a consecutive period of eight weeks. Body weight and blood glucose levels were monitored weekly throughout the drug intervention phase. This study found that the weight trend in the diabetes group was consistent with previous reports[25]. As shown in Fig. 2 (a), the weight gain percentage of CON group mice gradually increased during the experiment, while the weight gain percentage of DN group mice gradually decreased. Compared with the DN group, the weight gain percentage of the DAPA group gradually increased ($p < 0.05$). Figure 2(b) indicates that blood glucose levels remained stable in control mice, whereas a marked elevation was observed in model mice post-induction. Although blood glucose levels in treatment mice were comparable to those in model mice immediately after induction, they progressively declined following DAPA administration ($p < 0.05$). Renal function was assessed through the measurement of serum creatinine (Scr) and blood urea nitrogen (BUN) levels via respective assay kits. As depicted in Fig. 2(c-d), both Scr and BUN levels were notably higher in the model mice than in the control mice ($p < 0.05$). Nevertheless, Scr and BUN levels were significantly decreased in the DAPA-treated mice in comparison to the model mice ($p < 0.05$). We conducted a morphological examination of mouse kidneys and employed hematoxylin and eosin (HE) staining to assess pathological alterations. As depicted in Fig. 2(e), the glomeruli in the control group appeared plump with well-defined lumens and a distinct corticomedullary structure. In contrast, the model group displayed shrunken glomeruli, renal capsule gaps, reduced renal interstitium, and fused renal tubule lumens. Significantly, the renal status in the treatment group demonstrated marked enhancement in contrast to the model group. Renal blood flow alterations were assessed using color doppler ultrasound prior to sacrifice. In contrast to the control group, the renal blood flow volume and velocity in the model group were diminished, along with reductions in peak systolic velocity (Vsmax) and end-diastolic velocity (Vdmin), and an augmentation in the resistance index (RI) ($p < 0.05$). Conversely, in the treatment group, renal blood flow conditions improved, with enhancements in Vsmax and Vdmin, and a reduction in RI ($p < 0.05$). These findings are illustrated in Fig. 2(f-i).

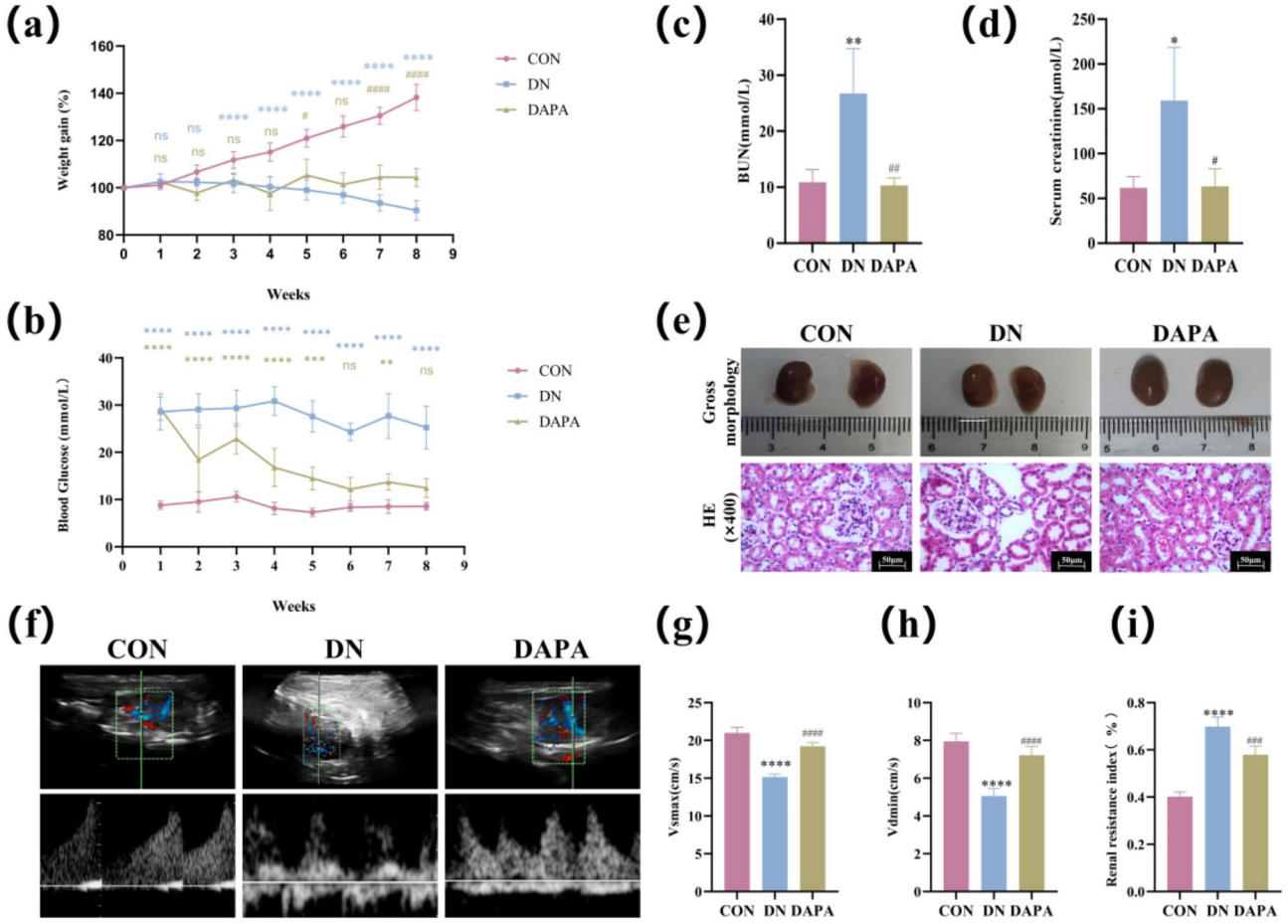

Fig. 2. Effect of DAPA on physiological indices, renal pathological morphology, and renal function in mice. (**a**) The percentage of original body weight of each group of mice during the experimental process. (**b**) The blood glucose levels of the mice. (**c**) The levels of BUN in mice. (**d**) The levels of Scr in mice. (**e**) The results of gross morphology and HE stains. Magnification: 400×. The scale bar represents a length of 50 μm. (**f**) The results of color doppler ultrasound. (**g**) The analysis of Vsmax. (**h**) The analysis of Vdmin. (**i**) The analysis of RI. ($^{*}p < 0.05$, $^{**}p < 0.01$, $^{***}p < 0.001$, $^{****}p < 0.0001$, $^{\#}p < 0.05$, $^{\#\#}p < 0.01$, $^{\#\#\#}p < 0.001$, $^{\#\#\#\#}p < 0.0001$, $^{ns}p > 0.05$).

Effect of DAPA on fibrosis in mice

To assess the degree of RF and the impacts of DAPA treatment, we employed periodic acid-Schiff (PAS), Masson's trichrome, and Sirius Red staining approaches. The results indicated that PAS staining disclosed exhibited proliferation of mesangial matrix and an augmentation in purple glycogen precipitation in the model group compared to the control group, which lessened subsequent to DAPA treatment. Compared to the CON group, there was a significant increase in the renal fibrosis level ($p < 0.001$). Treatment with DAPA for 8 weeks significantly ameliorated these histopathological changes, and renal fibrosis level ($p < 0.001$; Fig. 3a-c). Moreover, we extracted mRNA from mouse kidney tissue and carried out quantitative fluorescence analysis on several fibrotic markers, encompassing fibronectin (*FN*), alpha-smooth muscle actin (*α-SMA*), and type I collagen (*Col1*). As depicted in Fig. 3(d-f), the expression levels of *FN*, *α-SMA*, and *Col1* were conspicuously augmented in the renal tissue of the model group in contrast to the control group. Nevertheless, subsequent to DAPA treatment, the expression of these genes was significantly abated in comparison to the model group ($p < 0.05$). Subsequently, we extracted proteins from mouse tissues and conducted Western blotting experiments to evaluate the expression of TGF-β/Smad pathway proteins and fibrosis marker proteins following DN and DAPA treatment. As depicted in Fig. 3(g-m), the model group exhibited a significant upregulation in the expression of TGF-β1, Smad2, Smad3, p-Smad2, p-Smad3, FN, α-SMA, and Col1 in comparison to the control group ($p < 0.01$). Remarkably, the expression levels of these proteins were substantially reduced subsequent to DAPA treatment ($p < 0.01$).

Furthermore, we performed immunohistochemical staining on mouse kidney tissue to assess the expression of various fibrosis marker proteins. As illustrated in Fig. 3(n-u), the expression levels of TGF-β1, p-Smad2, p-Smad3, FN, α-SMA, Col1, and type III collagen (Col3) were conspicuously augmented in the kidneys of the model group in contrast to the control group. In contrast, the treatment group manifested a diminution in fibrosis deposition, coupled with a marked decline in the expression of fibrosis-related proteins ($p < 0.05$).

The influences of DAPA on inflammation, and ferroptosis in mice kidney tissue

We performed immunohistochemical staining on mouse kidney tissue to appraise the protein levels of the inflammatory factors nuclear factor kappa-B (NFκB) and interleukin-6 (IL-6). As demonstrated in Fig. 4(a-c), the expression of NFκB and IL-6 proteins in the model group was notably elevated compared to the normal control group ($p < 0.001$). Conversely, the DAPA group displayed a reduction in the expression of NFκB and IL-6 proteins in relation to the model group ($p < 0.001$). Furthermore, the measurement of iron content in mouse kidneys demonstrated that the model group exhibited significantly greater iron content in comparison to the control group ($p < 0.01$). Conversely, the tissue iron content in the treatment group decreased relative to the model group ($p < 0.05$), as depicted in Fig. 4(e). Prussian blue staining was employed to assess iron deposition in the kidneys. As shown in Fig. 4(d), iron deposition was absent in the kidney tissue of the control group. Conversely, iron deposition in the kidney tissue of the model group was augmented in comparison to the control group. Additionally, iron deposition in the DAPA treatment group was reduced compared to the model group. Additionally, Western Blotting experiments on ferroptosis-related proteins in mouse kidney tissue revealed that the expressions of ferritin heavy chain 1 (FTH1) and glutathion peroxidase 4 (GPX4) proteins were decreased in the model group in contrast to the normal control group, whereas the expression of COX2 protein was elevated ($p < 0.001$). In the DAPA group, the protein expressions of FTH1 and GPX4 augmented, and the expression of cyclooxygenase 2 (COX2) protein also rose compared to the model group ($p < 0.001$), as depicted in Fig. 4(f-i). Furthermore, we performed immunohistochemical staining of ferroptosis-related proteins, as shown in Fig. 4(j-n). The outcomes demonstrated that in the model group, the expression of GPX4 protein declined in contrast to the normal control group, whereas the expressions of COX2, NADPH oxidase 1 (NOX1), NADPH oxidase 4 (NOX4), and acyl-CoA synthetase long-chain family 4 (ACSL4) proteins escalated ($p < 0.001$). When comparing the DAPA group with the model group, an augmentation in GPX4 protein expression was noticed, along with a reduction in the expressions of COX2, NOX1, NOX4, and ACSL4 proteins ($p < 0.001$).

The influences of DAPA on oxidative stress in mice kidney tissue

Additionally, we evaluated the serum of mice for superoxide dismutase (SOD), glutathione (GSH), malondialdehyde (MDA), lactate dehydrogenase (LDH), catalase (CAT), and other biomarkers using respective assay kits. Our findings suggest that, in comparison to the control group, the model group presented with decreased concentrations of SOD, GSH, and CAT, whereas MDA and LDH levels were augmented ($p < 0.05$). In contrast, the treatment group exhibited increased levels of SOD, GSH, and CAT, along with reduced MDA and LDH levels ($p < 0.05$), as illustrated in Fig. 5(a-e). After confirming the antioxidant effect of DAPA, we further explored the potential mechanisms. Nuclear factor erythroid-derived 2-related factor 2 (Nrf2) plays a pivotal role in the antioxidant system. In response to oxidative stress, activated Nrf2 translocates into the nucleus, and thus leads to the expression of antioxidant response element (ARE)-driven genes, such as heme oxygenase-1 (HO-1). The results showed that the activation of Nrf2 signaling and the levels of antioxidant enzymes (HO-1) were obviously inhibited in DN mice, while DAPA treatment significantly activated Nrf2 signaling and increased the protein expression of HO-1 ($p < 0.001$) (Fig. 5f-h). We simultaneously detected the above indicators using immunohistochemistry and obtained the same results ($p < 0.001$) (Fig. 5i-k). These results indicated that the antioxidant effects of DAPA may be associated with the activation of Nrf2 signaling pathway.

The effects of DAPA on fibrosis, oxidative stress, and ferroptosis in HG-treated HK-2 cells

High glucose (HG) is the foundation and key of DN, sustained HG exposure to HK-2 cells will induce fibrosis and oxidative stress, further inducing the occurrence of ferroptosis. High concentration glucose insult promoted changes to HK-2 cells morphology, while DAPA and ferroptosis inhibitor ferrostatin-1 (Fer-1) treatment inhibited morphology changes (Fig. 6a). We further measured the levels of ROS and Fe^{2+} in HK-2 cells induced by high glucose (Fig. 6b). Compared with the NG group, the levels of ROS and Fe^{2+} in HK-2 cells treated with HG were significantly increased, and DAPA and Fer-1 could improve these phenomena (Fig. 6c, d). We next examined the expression of several important fibrosis, oxidative stress, and ferroptosis markers (Fig. 6e). The results showed that HG can induce an increase in the protein expression levels of α-SMA and TGF-β1 in HK-2 cells (Fig. 6f, g), promote renal tubular fibrosis, and reduce the protein expression levels of Nrf2, HO-1, and GPX4, thereby inducing cell ferroptosis (Fig. 6h-j). And DAPA and Fer-1 improve HG induced fibrosis, oxidative stress, and ferroptosis in HK-2 cells. Thus, it can be seen that DAPA can inhibit oxidative stress and ferroptosis of renal tubular epithelial cells under HG conditions, and improve fibrosis process.

The effects of DAPA on fibrosis, oxidative stress, and ferroptosis in Erastin-treated HK-2 cells

To further verify that the therapeutic effect of DAPA on HK-2 cells resulted from inhibition of Erastin-induced ferroptosis, Erastin was used as a specific inducer of ferroptosis. Also, in order to evaluate the association between ferroptosis and fibrosis, we added the TGF-β1 inhibitor SB431542 for intervention. After Erastin treatment, the number of cells decreased, cell morphology changed significantly (Fig. 7a), and the levels of ROS and Fe^{2+} increased significantly (Fig. 7b). Both DAPA and TGF-β1 inhibitors can improve this phenomenon to a certain extent (Fig. 7c, d). The levels of fibrosis markers α-SMA and TGF-β1 increased after Erastin treatment (Fig. 7e-g). In addition, when cellular oxidative stress is significantly enhanced, antioxidant capacity may be weakened. After Erastin treatment, the protein expression levels of Nrf2, HO-1, and GPX4 were significantly reduced (Fig. 7h-j). DAPA and TGF-β1 inhibitors can improve Erastin induced fibrosis and ferroptosis. The above results indicate that the protective effect of DAPA on the kidneys is not limited to lowering blood sugar. DAPA can also inhibit ferroptosis in kidney cells by improving oxidative stress and intervening in the progression of renal fibrosis.

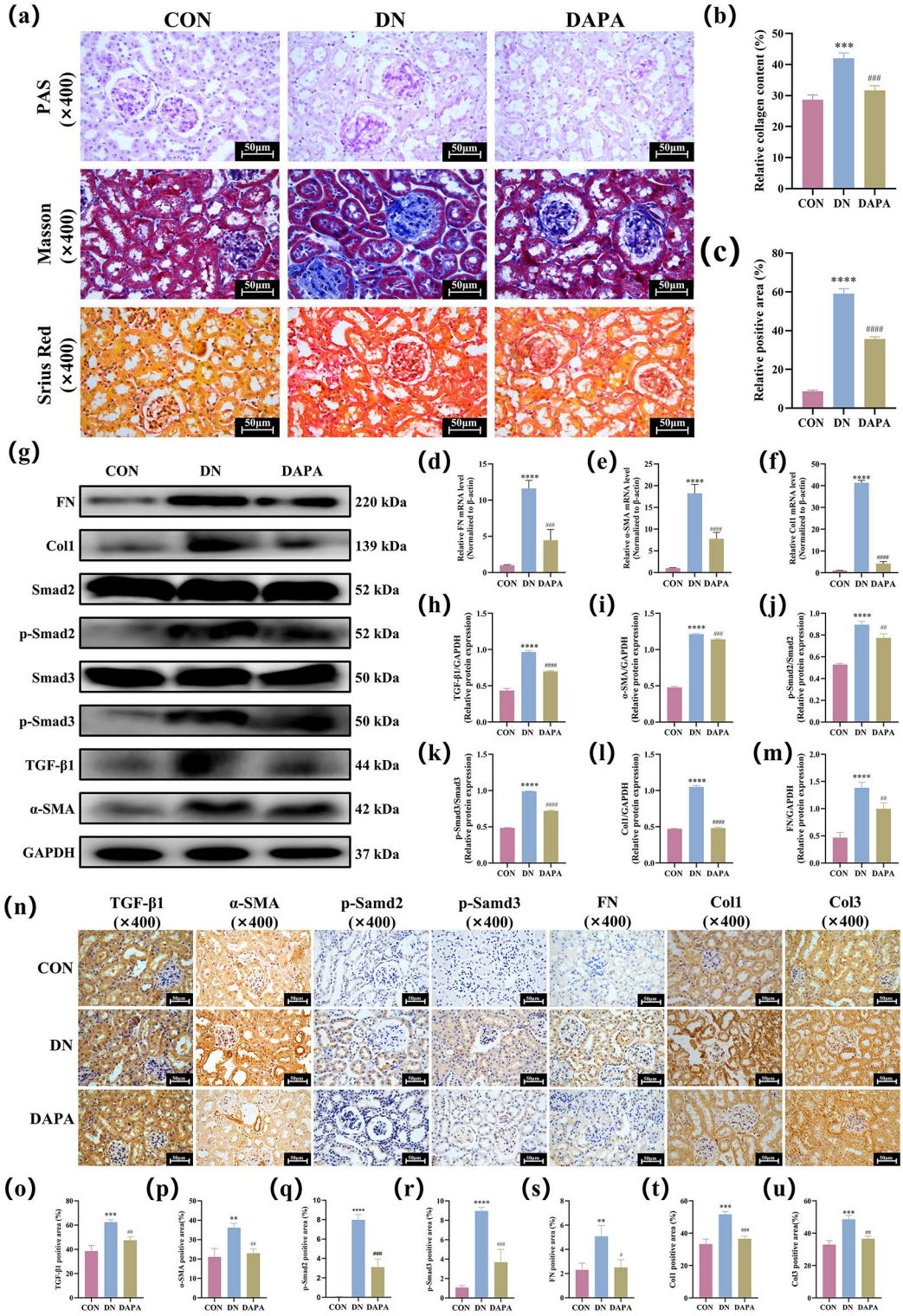

Target results of DAPA, DN fibrosis, and ferroptosis

We integrated the chemical structure of DAPA, obtained from PubChem (https://pubchem.ncbi.nlm.nih.gov/), into the SwissTargetPrediction database (http://swisstargetprediction.ch/) for target screening, filtering for results specific to "Homo sapiens" with a probability threshold greater than 0. We also utilized the CTD (https://ctdbase.org/) and PharmMapper databases (https://www.lilab-ecust.cn/pharmmapper/) to refine our target predictions, converting gene names through UniProt (https://www.uniprot.org/), yielding a total of 413 targets. Additionally, we collected 3011 targets associated with diabetic RF from the GeneCards database (https://www.genecards.org/). Furthermore, we identified 720 ferroptosis-related genes using the FerrDbV2 database (http://zhounan.org/ferrdb/current).

◀**Fig. 3**. Effect of DAPA on fibrosis in mice. (**a**) PAS, Masson, and Sirius red staining. Magnification: 400×. The scale bar represents a length of 50 μm. (**b**) Semi-quantitative analysis of Masson staining. (**c**) Semi-quantitative analysis of Sirius red staining. (**d**) The mRNA levels of *FN*. (**e**) The mRNA levels of *α-SMA*. (**f**) The mRNA levels of *Col1*. (**g**) Detection of TGF-β/Smad pathway marker protein by WB. (**h**) The WB analysis of TGF-β1/GAPDH. (**i**) The WB analysis of α-SMA/GAPDH. (**j**) The WB analysis of p-Smad2/Smad2. (**k**) The WB analysis of p-Smad3/Smad3. (**l**) The WB analysis of Col1/GAPDH. (**m**) The WB analysis of FN/GAPDH. (**n**) Detection of TGF-β/Smad pathway marker protein by IHC. Magnification: 400×. The scale bar represents a length of 50 μm. (**o**) The IHC analysis of TGF-β1. (**p**) The IHC analysis of α-SMA. (**q**) The IHC analysis of p-Smad2. (**r**) The IHC analysis of p-Smad3. (**n**) The IHC analysis of relative fibrosis protein. Magnification: 400×. The scale bar represents a length of 50 μm. (**s**) The IHC analysis of FN. (**t**) The IHC analysis of Col1. (**u**) The IHC analysis of Col3. ($^{*}p<0.05$, $^{**}p<0.01$, $^{***}p<0.001$, $^{****}p<0.0001$, $^{\#}p<0.05$, $^{\#\#}p<0.01$, $^{\#\#\#}p<0.001$, $^{\#\#\#\#}p<0.0001$).

Prediction results of potential targets for DAPA in targeting ferroptosis to treat RF

The targets identified in Sect. 3.4 for DAPA, RF, and ferroptosis were represented in a Venn diagram, revealing a total of 53 intersecting targets, as depicted in Fig. 8a.

Construction of protein-protein interaction (PPI) network and core target screening

The intersecting targets were input into the STRING database (https://cn.string-db.org/) to extract PPI information in Fig. 8(b), and Cytoscape software was employed to visualize the PPI network diagram, as shown in Fig. 8(c). Utilizing cytoHubba calculations, the top 10 core targets based on the maximum clique centrality (MCC) method, including caspase-3 (CASP3), estrogen receptor 1 (ESR1), mammalian target of rapamycin (MTOR), nuclear factor erythroid 2-related factor 2 (NFE2L2), prostaglandin-endoperoxide synthase 2 (PTSG2), Rela proto-oncogene (RELA), Src proto-oncogene (SRC), signal transducer and activator of transcription 3 (STAT3), tumor necrosis factor (TNF), and tumor protein 53 (TP53) were identified, as illustrated in Fig. 8(d). Meanwhile, showed as Fig. 8(e-n), mRNA expression of *TNF*, *TP53*, *CASP3*, *STAT3*, *PTGS2*, *RELA* and *SRC* were upregulated and *MTOR*, *NFE2L2*, and *ESR1* were downregulated in DN group compared with CON group.

The results of the gene ontology (GO), and the Kyoto encyclopedia of genes and genomes (KEGG) functional enrichment analysis

Employing the DAVID database (https://david.ncifcrf.gov/), SRplot (http://www.bioinformatics.com.cn/), and the Omicshare online tool (https://www.omicsshare.com/tools/) for visualization, a total of 301 data points were obtained in GO analysis with a significance threshold of $p<0.05$. This analysis disclosed 455 biological process (BP) entries, mainly encompassing the positive modulation of transcription from RNA polymerase II promoter, positive regulation of gene expression, and cellular response to hypoxia. Additionally, as shown in Fig. 8o-p. There were 46 cellular component (CC) entries, mainly related to nucleoplasm, nuclei, and cytosol, as well as 78 molecular function (MF) entries, which primarily involved enzyme binding, nuclear receptor activity, and identical protein binding. Figure 8q illustrates that in the KEGG pathway analysis, the mechanism by which DAPA targets ferroptosis to treat DN fibrosis may be associated with several signaling pathways, encompassing the MAPK signaling pathway, TNF signaling pathway, FoxO signaling pathway, and TGF-β signaling pathway. Additionally, a "drug-target-pathway-disease" network diagram has been constructed, presented in Fig. 8r.

The results of molecular Docking

The top 10 core target genes were subjected to molecular docking with DAPA, resulting in a top 3 of docking outcomes showed in Fig. 8(s-u). Among these, the strongest interaction was observed between DAPA and PTGS2, which exhibited a docking score of -9.6 kcal/mol. For further details, refer to Table 1.

Discussion

DN is a prevalent complication associated with diabetes and has become the predominant cause of chronic renal failure. To date, effective treatment strategies for DN remain elusive[26,27]. For patients with end-stage DN, the primary management options are hemodialysis and symptomatic therapy, which place substantial economic and psychological burdens on both individuals and society[28]. The pathological hallmark of DN is RF, which stems from sustained inflammatory responses triggered by hyperglycemia and the accumulation of macromolecular glucose in the bloodstream[29]. Consequently, the primary research objectives in the treatment of DN center on inhibiting inflammation and oxidative stress, improving glomerular hyperfiltration, and curbing the progression of fibrosis.

In recent years, ferroptosis has been associated with the initiation and advancement of DN[30]. This process potentially encompasses pathological changes such as inflammation, oxidative stress, and fibrosis, which disrupt the structure and function of renal cells and foster disease progression[31]. Therefore, conducting in-depth research on the regulatory factors and signaling pathways involved in ferroptosis is vital for elucidating the pathogenesis of DN and identifying new therapeutic targets.

DAPA is hailed as a "new star in glucose-lowering medications," with numerous studies attesting to its clinical benefits for renal pathology. DAPA not only effectively regulates blood glucose levels but also significantly enhances renal function while maintaining a high safety profile, making it a promising candidate for clinical adoption[32,33]. Although many clinicians have begun to prescribe this class of medication, the underlying mechanisms of its action remain to be fully elucidated. Given the limited understanding of the underlying mechanisms associated with this class of medications, as well as the potential for unaddressed off-target

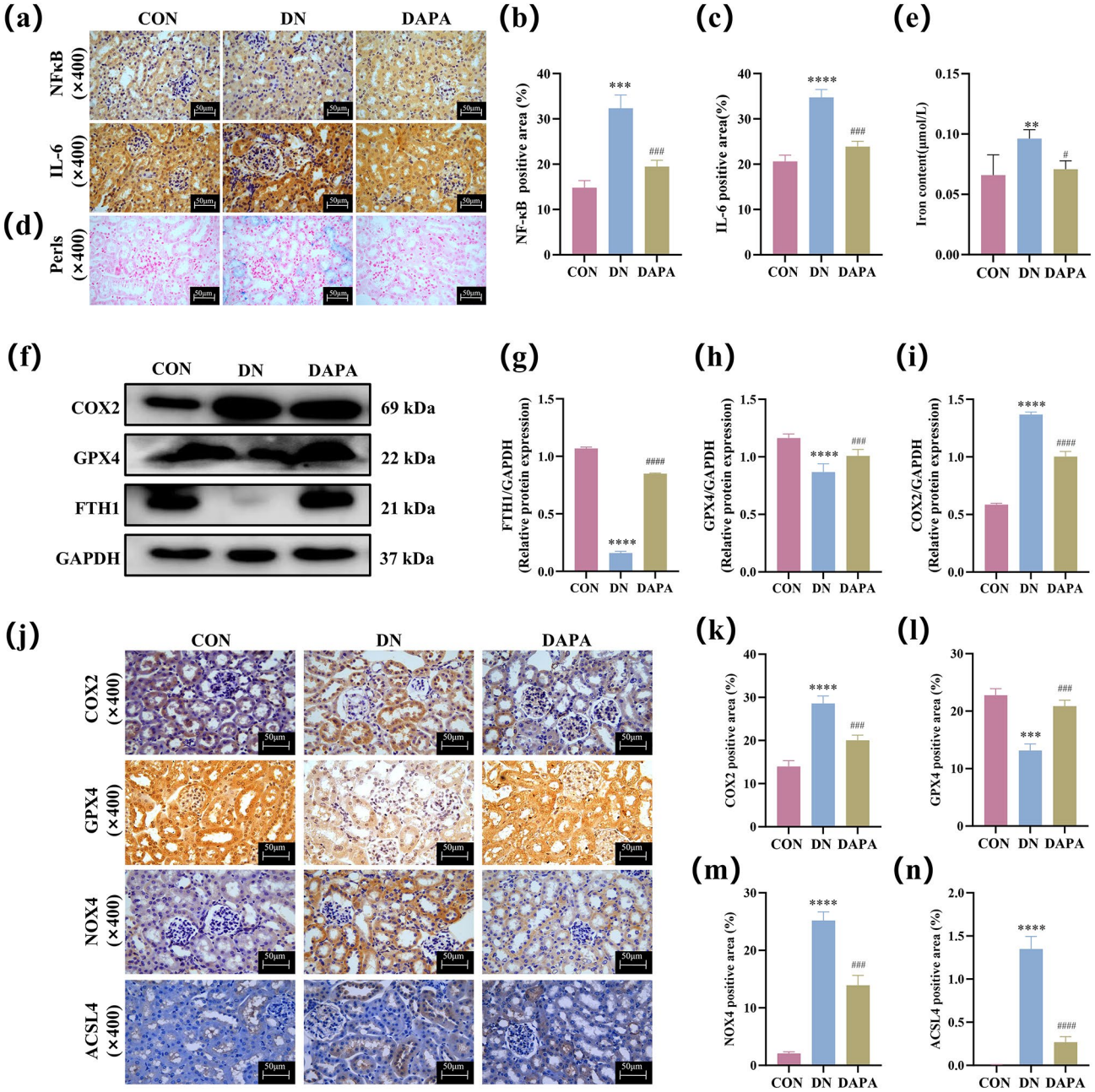

Fig. 4. The effects of DAPA on inflammation, oxidative stress, and ferroptosis in mice kidney tissue. (**a**) Detection of NFκB and IL-6 by IHC. Magnification: 400×. The scale bar represents a length of 50 μm. (**b**) The IHC analysis of NFκB. (**c**) The IHC analysis of IL-6. (**d**) Prussian blue staining. Magnification: 400×. The scale bar represents a length of 50 μm. (**e**) The levels of iron content. (**f**) The WB analysis of ferroptosis marker protein. (**g**) The WB analysis of FTH1/GAPDH. (**h**) The WB analysis of GPX4/GAPDH. (**i**) The WB analysis of COX2/GAPDH. (**j**) The IHC analysis of ferroptosis. Magnification: 400×. The scale bar represents a length of 50 μm. (**k**) The IHC analysis of COX2. (**l**) The IHC analysis of GPX4. (**m**) The IHC analysis of NOX4. (**n**) The IHC analysis of ACSL4. ($^{*}p<0.05$, $^{**}p<0.01$, $^{***}p<0.001$, $^{****}p<0.0001$, $^{\#}p<0.05$, $^{\#\#}p<0.01$, $^{\#\#\#}p<0.001$, $^{\#\#\#\#}p<0.0001$).

effects and the limitations inherent in drug repurposing, such as that of DAPA for the treatment of RF, more comprehensive research is urgently needed[18,34,35].

Our team established a diabetic mouse model through STZ injection and employed DAPA for intervention to evaluate its efficacy in experimental diabetes. Post-DAPA administration, we observed that the weight of diabetic mice was effectively managed without significant loss, and blood glucose levels were significantly regulated. Renal ultrasound examinations were conducted to monitor morphological changes and blood flow in the mice, while Scr and urea nitrogen levels were measured, confirming that DAPA can effectively alleviate renal injury induced by diabetes. Histological techniques, including HE, Masson's trichrome, Sirius red, and PAS

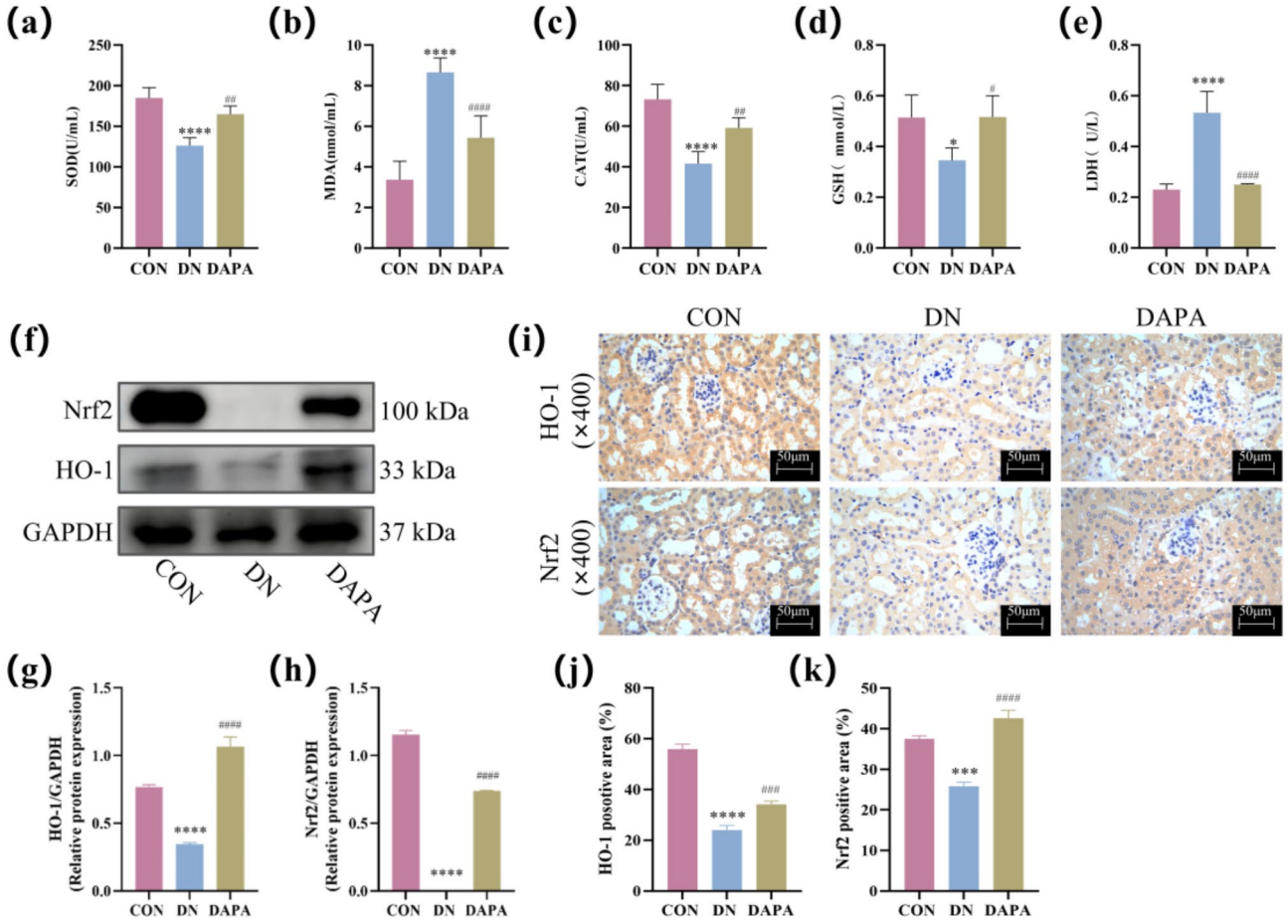

Fig. 5. The effects of DAPA on oxidative stress in mice kidney tissue. (**a**) The levels of SOD. (**b**) The levels of GSH. (**c**) The levels of MDA. (**d**) The levels of LDH. (**e**) The levels of CAT. (**f**) Detection of Nrf2/HO-1 pathway marker protein by WB. (**g**) The WB analysis of Nrf2/GAPDH. (**h**) The WB analysis of HO-1/GAPDH. (**i**) Detection of Nrf2/HO-1 pathway by IHC. Magnification: 400×. The scale bar represents a length of 50 μm. (**j**) The IHC analysis of Nrf2. (**k**) The IHC analysis of HO-1. ($^{*}p < 0.05$, $^{**}p < 0.01$, $^{***}p < 0.001$, $^{****}p < 0.0001$, $^{\#}p < 0.05$, $^{\#\#}p < 0.01$, $^{\#\#\#}p < 0.001$, $^{\#\#\#\#}p < 0.0001$).

staining of mouse renal tissue sections, demonstrated that DAPA can reduce the extent of RF in diabetic mice. Using assay kits for MDA, GSH, SOD, immunohistochemistry, and Western blotting, we observed that DAPA reduced oxidative stress levels in the mice. Furthermore, through experiments including Prussian blue staining, immunohistochemistry, and Western blotting, we confirmed that DAPA can inhibit ferroptosis. Additionally, by measuring TGF-β1 and its downstream fibrosis-related proteins, we established that DAPA can inhibit ferroptosis and regulate RF through the TGF-β/Smad pathway. Combining the findings of our in vivo experiments and previous studies, DAPA can improve the fibrosis of diabetes and its complications DN through TGF-β/Smad and other related signaling pathways[9,10,36–39]. However, research on whether DAPA targets ferroptosis through the TGF-β/Smad signaling pathway to improve RF has not yet been conducted, which is also the innovation of our study. In order to investigate the specific mechanism of ferroptosis in the improvement of RF by DAPA, we conducted a series of in vitro experiments and treated HK-2 cells with ferroptosis inhibitors and inducers. The results showed that DAPA could inhibit oxidative stress and ferroptosis in renal tubular epithelial cells under HG and Erastin conditions, and improve the fibrosis process.

Network pharmacology offers significant application potential and theoretical importance in drug development and disease treatment. With advancements in databases, we conducted a comprehensive analysis of drugs, diseases, and ferroptosis using network pharmacology. Our screening identified 10 core targets and verified at the mRNA level. Molecular docking results indicated that PTGS2 exhibited the highest binding affinity to DAPA, followed by SRC and NFE2L2. PTGS2, also known as COX2, is a primary target of non-steroidal anti-inflammatory drugs and plays a critical role in various pathological processes, including inflammatory responses, cell proliferation, and apoptosis, thereby serving as a marker molecule for ferroptosis. Studies have demonstrated that during the onset of DN, an excess of ferrous ions within cells generates significant lipid peroxidation, leading to an imbalance in intracellular lipid peroxidation metabolism. This imbalance results in the production of numerous lipid-derived ROS, which induce cell death[14,40]. Therefore, based on animals experimental findings, it is suggested that DAPA may mitigate intracellular ROS accumulation by enhancing PTGS2 activity and

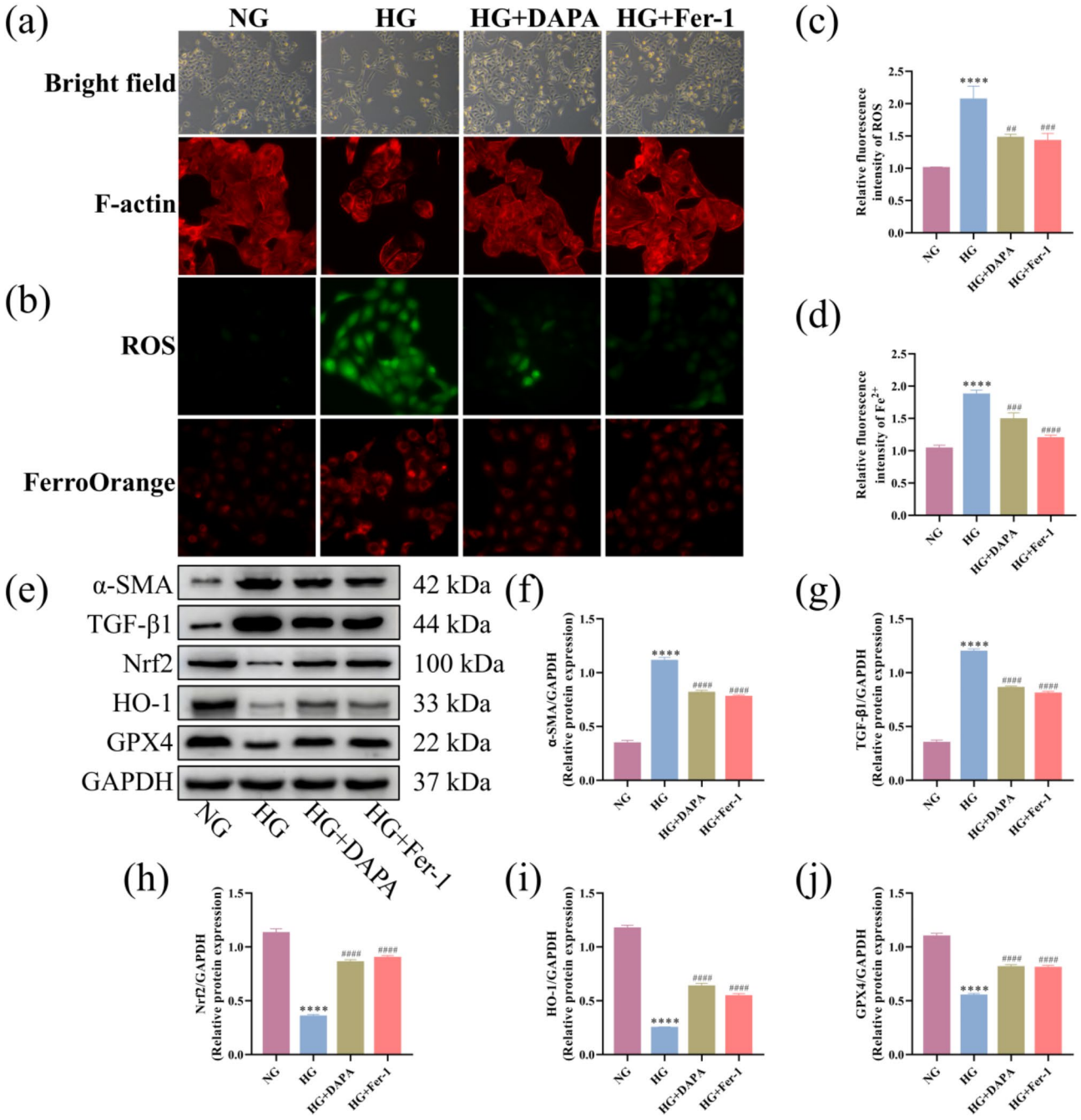

Fig. 6. The effects of DAPA on fibrosis, oxidative stress, and ferroptosis in HG-treated HK-2 cells. (**a**) Morphological changes and F-actin of HK-2 cells treated with HG. (**b**) ROS and Fe^{2+} levels of HK-2 cells treated with HG. (**c**) Semi-quantitative analysis of ROS levels of HK-2 cells treated with HG. (**d**) Semi-quantitative analysis of Fe^{2+} levels of HK-2 cells treated with HG. (**e**) The protein levels of α-SMA, TGF-β1, Nrf2, HO-1 and GPX4 in HG-treated HK-2 cells were measured by Western blot. (**f**) The WB analysis of α-SMA/GAPDH. (**g**) The WB analysis of TGF-β1/GAPDH. (**h**) The WB analysis of Nrf2/GAPDH. (**i**) The WB analysis of HO-1/GAPDH. (**j**) The WB analysis of GPX4/GAPDH. ($^{*}p<0.05$, $^{**}p<0.01$, $^{***}p<0.001$, $^{****}p<0.0001$, $^{\#}p<0.05$, $^{\#\#}p<0.01$, $^{\#\#\#}p<0.001$, $^{\#\#\#\#}p<0.0001$).

increasing GPX4 expression, thereby delaying lipid peroxidation, inhibiting ferroptosis, and improving DN. Additionally, NFE2L2, also known as Nrf2, is a critical cell-protective gene that regulates essential antioxidant and stress-response genes and plays a role in inhibiting ferroptosis[41]. KEGG pathway enrichment results indicate that the MAPK signaling pathway, TNF signaling pathway, and FoxO signaling pathway may serve as potential mechanisms through which DAPA targets ferroptosis in the treatment of DN fibrosis. The TGF-β signaling pathway is also implicated, with TGF-β1 playing a pivotal role in the fibrosis process by regulating various upstream and downstream factors. Therefore, we hypothesize that DAPA maintains stable blood glucose levels

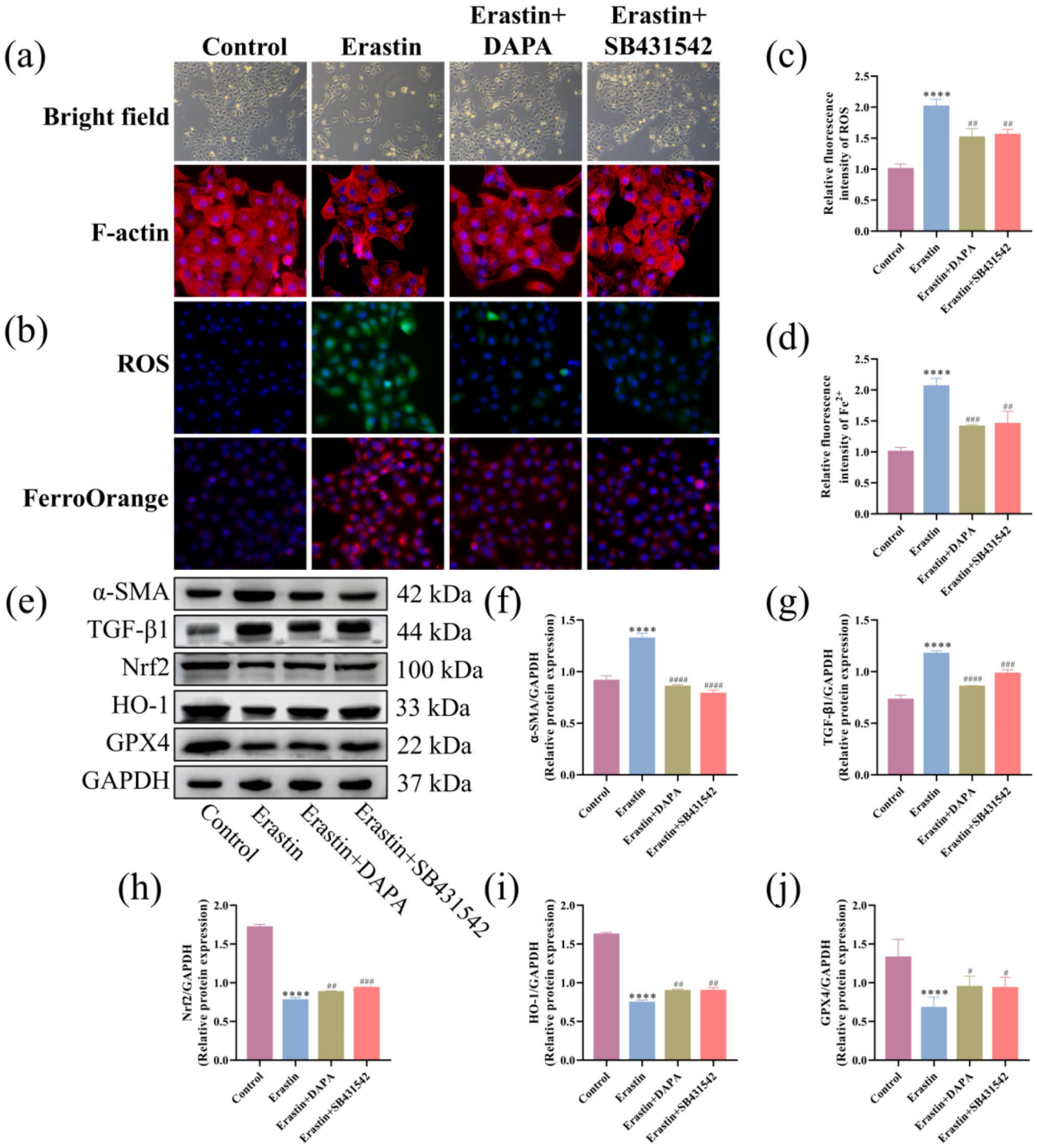

Fig. 7. The effects of DAPA on fibrosis, oxidative stress, and ferroptosis in Erastin-treated HK-2 cells. (**a**) Morphological changes and F-actin of HK-2 cells treated with Erastin. (**b**) ROS and Fe^{2+} levels of HK-2 cells treated with Erastin. (**c**) Semi-quantitative analysis of ROS levels of HK-2 cells treated with Erastin. (**d**) Semi-quantitative analysis of Fe^{2+} levels of HK-2 cells treated with Erastin. (**e**) The protein levels of α-SMA, TGF-β1, Nrf2, HO-1 and GPX4 in Erastin-treated HK-2 cells were measured by Western blot. (**f**) The WB analysis of α-SMA/GAPDH. (**g**) The WB analysis of TGF-β1/GAPDH. (**h**) The WB analysis of Nrf2/GAPDH. (**i**) The WB analysis of HO-1/GAPDH. (**j**) The WB analysis of GPX4/GAPDH. ($^{*}p < 0.05$, $^{**}p < 0.01$, $^{***}p < 0.001$, $^{****}p < 0.0001$, $^{\#}p < 0.05$, $^{\#\#}p < 0.01$, $^{\#\#\#}p < 0.001$, $^{\#\#\#\#}p < 0.0001$).

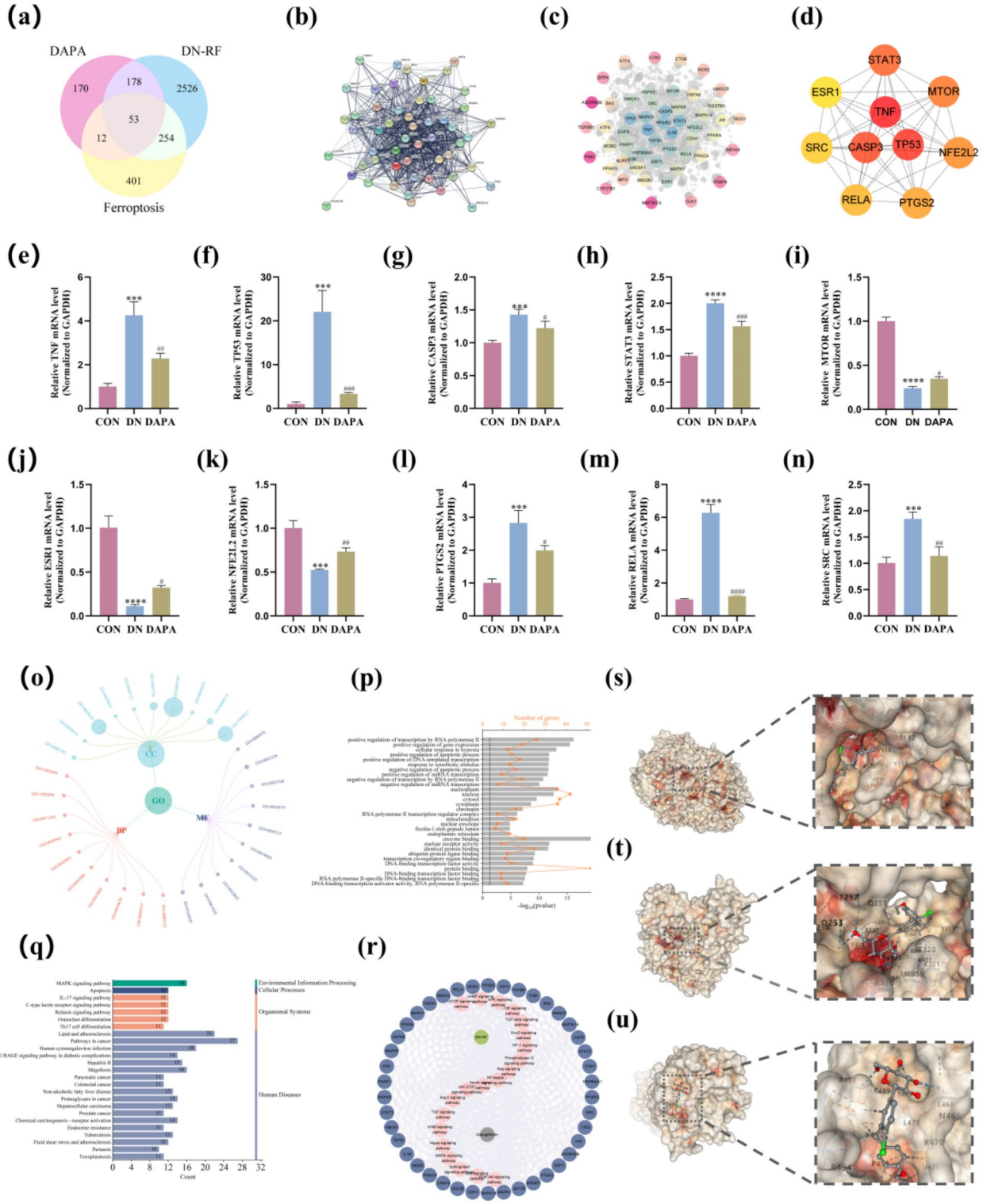

Fig. 8. Network pharmacology and macromolecular docking. (**a**) A Venn diagram. (**b**) PPI Network. (**c**) The visualization results of the PPI network diagram. (**d**) The top 10 core targets. (**e**) The mRNA levels of *TNF*. (**f**) The mRNA levels of *TP53*. (**g**) The mRNA levels of *CASP3*. (**h**) The mRNA levels of *STAT3*. (**i**) The mRNA levels of *MTOR*. (**j**) The mRNA levels of *NFE2L2*. (**k**) The mRNA levels of *PTGS2*. (**l**) The mRNA levels of *RELA*. (**m**) The mRNA levels of *SRC*. (**n**) The mRNA levels of *ESR1*. (**o**) GO analysis by three-tier dependency circle diagram. (**p**) GO analysis by double X-axis bar and line chart. (**q**) KEEG analysis. (**r**) The "drug-target-pathway-disease" network diagram. (**s**) The molecular docking result of PTSG2 with DAPA. (**t**) The molecular docking result of SRC with DAPA. (**u**) The molecular docking result of NEF2L2 with DAPA. ($^{*}p < 0.05$, $^{**}p < 0.01$, $^{***}p < 0.001$, $^{****}p < 0.0001$, $^{\#}p < 0.05$, $^{\#\#}p < 0.01$, $^{\#\#\#}p < 0.001$, $^{\#\#\#\#}p < 0.0001$).

Number	Receptor	Ligands	Vina score	Center (x, y, z)	Docking size (x, y, z)
1	CASP3	dagliflozin	-6.6	-1, 122, 112	23, 23, 23
2	ESR1	dagliflozin	-7.5	13, 50, 25	24, 24, 24
3	MTOR	dagliflozin	-7.9	13, 4, 58	23, 23, 23
4	NFE2L2	dagliflozin	-9.0	-2, 5, 18	35, 35, 33
5	PTSG2	dagliflozin	-9.6	46, 36, 204	30, 35, 23
6	RELA	dagliflozin	-8.8	42, -13, 13	23, 23, 23
7	SRC	dagliflozin	-9.4	18, 25, 57	23, 23, 23
8	STAT3	dagliflozin	-7.8	5, 32, 20	23, 23, 23
9	TNF	dagliflozin	-6.8	2, 30, -11	23, 23, 23
10	TP53	dagliflozin	-6.5	30, 32, 110	23, 23, 23

Table 1. Results of molecular Docking of dagliflozin-core targets.

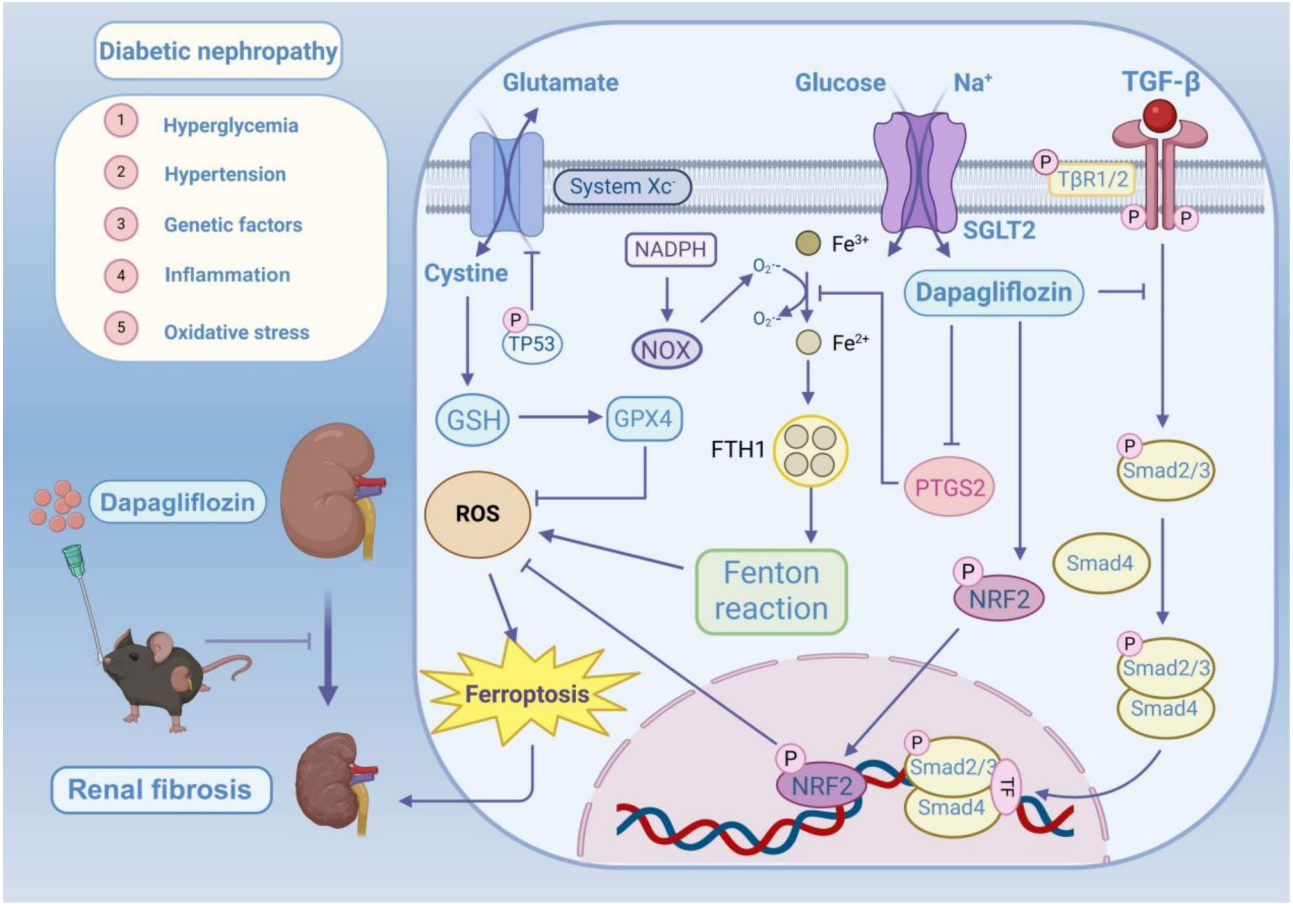

Fig. 9. The possible mechanism of DAPA inhibits ferroptosis and ameliorates renal fibrosis in diabetic mice (Created by biorender).

through its potent glucose-lowering effect, thereby inhibiting inflammation and oxidative stress. Furthermore, DAPA exerts an inhibitory effect on ferroptosis by regulating genes such as PTGS2 and NFE2L2, and improves RF through the TGF-β/Smad pathway. For further details, please refer to the accompanying mechanism diagram (Fig. 9).

Conclusion

In conclusion, this study demonstrates that DAPA exerts significant renal protective effects in the context of DN by ameliorating renal fibrosis and inhibiting ferroptosis. The findings illustrate that DAPA not only improves renal function, as evidenced by reduced serum creatinine and blood urea nitrogen levels in a streptozotocin-induced diabetic mouse model, but also mitigates histopathological changes associated with DN, including glomerulosclerosis and interstitial fibrosis.

Furthermore, DAPA was shown to act at the cellular level by inhibiting high glucose-induced ferroptosis and oxidative stress in HK-2 cells, thereby reducing levels of ROS and iron deposition while enhancing the expression of antioxidant markers. Molecular docking and network pharmacology analyses revealed that DAPA interacts with key regulatory pathways, notably the Nrf2 and TGF-β signaling pathways, which are crucial in mediating its anti-fibrotic and anti-ferroptotic effects.

These results provide compelling evidence for the therapeutic potential of DAPA in managing DN through multifaceted mechanisms. The study not only reinforces the role of DAPA as a SGLT2 inhibitor but also highlights its relevance in targeting ferroptosis, thereby offering new insights for the development of targeted therapeutic strategies against DN. Future research is warranted to explore the broader applications of DAPA in other diabetic complications and to assess its long-term safety and efficacy in clinical settings.

Materials and methods

Reagents and chemicals, and instruments

DAPA (Janssen Ortho, H20170375), Isoflurane (Guangshengyuan Biotech, 20200701), Pentobarbital sodium (Beijing Chemical Reagent Company, 020919), Scr, BUN, GSH, MDA, LDH, SOD, CAT, and tissue iron content were procured from Nanjing Jiancheng Bioengineering Institute (C011-2-1, C013-2-1, A006-2-1, A003-1-2, A020-1-2, A001-3-2, A007-2-1, A039-2-1). HE staining solution, modified Masson's trichrome staining kit, Prussian blue staining kit and Dapagliflozin were sourced from Solarbio Science & Technology Co., Ltd. (G1140, G1105, G1346, 1220). The Sirius red staining kit was obtained from Maokang Biological Company (MM1004), and the PAS staining kit, ROS Assay Kit, Actin-Tracker Red-Rhodamine, Erastin, and SB431542 were acquired from Beyotime Biotechnology (C0142S, S0033S, C2207S, SC0224, SF7890). FerroOrange (Dojindo Laboratories, Japan, F374). Ferrostatin-1 (MCE, HY-100579). Antibodies for Col1, Col3, α-SMA, FN, TGF-β1, smad3, p-smad3, smad2, p-smad2, GPX4, NOX4, COX2, ACLS4, FTH1, NOX1, Nrf2 and HO-1 were sourced from Affinity Biosciences (AF7001, AF0136, AF1032, AF5335, AF1027, AF6362, AF3362, AF6449, AF3450, DF6701, DF6924, AF7003, DF12141, DF6278, DF8684, AF0639, AF5393). GAPDH was obtained from Abcam (ab9485), and NFκB and IL-6 were purchased from Wanleibio (WL01980, WL02841). Horseradish peroxidase-conjugated goat anti-rabbit IgG was supplied by Zhongshan Golden Bridge Biotechnology (ZB-2301). The OMEGA kit was sourced from Omega Biotek (USA), and the Reverse Transcription cDNA Synthesis kit was obtained from Roche Diagnostics (Germany, A722074). Equipment utilized in the study included an ultrasound machine (Esaote MyLabTM, Italy), an Accu-Chek blood glucose meter (Roche Diagnostics, Switzerland), a microplate reader (Molecular Devices, USA), an electrophoresis apparatus (Bio-Rad, USA), a real-time PCR system (Thermo Fisher Scientific, USA), an S100 PCR automated analyzer (Bio-Rad, USA), and a Molecular Imager gel documentation system (Bio-Rad, USA).

Animals

This investigation engaged eight-week-old male C57BL/6J mice, distinguished as specific pathogen-free (SPF), with weights ranging from 18 to 22 g, procured from the Comparative Medicine Center of Mudanjiang Medical University (Animal License No. SCXK (Heilongjiang) 2019-003). The mice were housed under meticulously controlled conditions, experiencing a 12-hour light-dark cycle, receiving appropriate nutrition, and resting upon comfortable bedding, followed by a one-week acclimatization period. All animal experimentation was received approval from the Institutional Animal Care and Use Committee (IACUC) of Mudanjiang Medical University (Animal Welfare and Ethics Review No. IACUC-20230314-71). The administration and utilization of mice align with the pertinent directives of the US National Institutes of Health. All experiments were performed following the ARRIVE guidelines (http://arriveguidelines.org) to report animal experiments.

To create a diabetic mouse model, a single dose of 50 $mg{\cdot}kg^{-1}$ streptozotocin (STZ) was administered intraperitoneally for four consecutive days. Blood glucose levels were monitored, and a model was considered successful if blood glucose levels exceeded 16.7 $mmol{\cdot}L^{-1}$ for three consecutive days. Control mice received an equal volume of citrate buffer at pH 4.4. The diabetic mice were then randomly assigned to either the diabetes group (DN group, $n=6$) or the Dapagliflozin (DAPA) treatment group (DAPA group, 10 $mg{\cdot}kg^{-1}{\cdot}d^{-1}$, $n=6$), the drug solution was freshly prepared, dissolved, and diluted in physiological saline[36]. Mice in both the control (CON) and DN-treated groups were given the same volume of physiological saline by mouth for eight weeks. Body weight and blood glucose levels were recorded weekly. After the treatment period, the mice were first anesthetized with 2% isoflurane for a renal ultrasound examination. Subsequently, they received 0.3% pentobarbital sodium (30 mg/kg) via intraperitoneal injection for further anesthesia. Blood was collected through cardiac puncture, and euthanasia was performed via cervical dislocation. Blood samples and both kidneys were collected, with a portion of the kidney fixed in 4% formalin for histological analysis, while the remainder was stored at -80 °C for molecular biology assessments.

Culture and treatment of renal tubular epithelial cells

Cultivate HK-2 cells in DMEM medium supplemented with 10% fetal bovine serum and 1% penicillin (100 U/ml)–streptomycin (100 μg/ml), and incubate them in a humidified atmosphere of 5% CO_2 and 95% air at 37 °C.

HK-2 cells were treated with normal glucose (NG, 5.5 mM), high glucose (35mM, HG), high glucose with either DAPA (10 μM, HG + DAPA), or Ferrostatin-1 (1 μM, HG + Fer-1). Establish the model after 48 h.

HK-2 cells were treated with normal glucose (NG, 5.5 mM), Erastin (5 μM, Erastin), Erastin with either DAPA (10 μM, Erastin + DAPA), or SB431542 (10 μM, Erastin + SB431542). The model was established 24 h later.

Planted an appropriate amount of cells into a 6 well plate, and after the cells adhered to the wall, perform relevant treatments on the cells. Wash twice with PBS, observed and photographed under an optical microscope.

GENE	Forward Sequence	Reverse Sequence
FN	CAGTGACTGGAGAGACTG	TGCCAGGGGAACATAGGCT
Col1	TAGGCCATTGTGTATGCAGC	ACATGTCAGCTTTGTGGACC
α-SMA	CTGACAGAGGCACCACTGAA	CATCTCCAGAGTCCAGCACA
β-actin	AACTCCATCATGAAGTGTGA	ACTCCTGCTTGCTGATCCAC
CASP3	GGAGTCTGACTGGAAAGCCGAA	CTTCTGGCAAGCCATCTCCTCA
ESR1	TCTGCCAAGGAGACTCGCTACT	GGTGCATTGGTTTGTAGCTGGAC
MTOR	AGAAGGGTCTCCAAGGACGACT	GCAGGACACAAAGGCAGCATTG
NFE2L2	CAGCATAGAGCAGGACATGGAG	GAACAGCGGTAGTATCAGCCAG
PTSG2	GCGACATACTCAAGCAGGAGCA	AGTGGTAACCGCTCAGGTGTTG
RELA	TCCTGTTCGAGTCTCCATGCAG	GGTCTCATAGGTCCTTTTGCGC
SRC	GTTGCTTCGGAGAGGTGTGGAT	CACCAGTTTCTCGTGCCTCAGT
STAT3	AGGAGTCTAACAACGGCAGCCT	GTGGTACACCTCAGTCTCGAAG
TNF	GGTGCCTATGTCTCAGCCTCTT	GCCATAGAACTGATGAGAGGGAG
TP53	CCTCAGCATCTTATCCGAGTGG	TGGATGGTGGTACAGTCAGAGC
GAPDH	CATCACTGCCACCCAGAAGACTG	ATGCCAGTGAGCTTCCCGTTCAG

Table 2. List of primers used for qRT-PCR.

F-actin staining

Cells were seeded into confocal dishes and allowed to adhere before further processing. After two washes with phosphate-buffered saline (PBS), the cells were fixed in a 3.7% formaldehyde solution prepared in PBS at room temperature for 15 min. Following fixation, the cells were washed three times with PBS containing 0.1% Triton X-100, with each wash lasting 5 min. To stain F-actin and nuclei, Actin-Tracker Red and DAPI were diluted in PBS containing 0.1% Triton X-100 at ratios of 1:100 and 1:1000, respectively. A total of 200 μL of the staining solution was added to each dish and incubated at room temperature in the dark for 30 min. After incubation, the cells were washed three times with PBS containing 0.1% Triton X-100, each wash lasting 5 min. Finally, the cells were observed and photographed under a fluorescence microscope.

Biochemical index detection

Blood was obtained from the ocular globe and centrifuged to acquire the serum supernatant. The levels of Scr and BUN were measured using respective assay kits in accordance with the manufacturer's protocols.

HE, Masson, PAS, and Sirius red staining

Staining Paraffin-embedded sections underwent deparaffinization and dehydration. For HE staining, sections were stained with hematoxylin for 5 min, differentiated with 3% hydrochloric acid ethanol, and then blued in tap water. Subsequently, they were stained with eosin for 5 s, dehydrated, and mounted. Masson's trichrome, PAS, and Sirius Red staining were carried out following the manufacturer's instructions, followed by dehydration, mounting, and microscopic examination.

Prussian blue staining for renal iron deposition

Paraffin-embedded sections were habitually dehydrated and stained with Perls' operational solution for 15 min. Subsequently, after rinsing, the sections were stained with nuclear fast red for 10 min, rinsed anew, dehydrated, mounted, and observed beneath a microscope.

Detection of oxidative stress-related indicators

Blood was gathered from the medial canthus, and the specimens were centrifuged to obtain the supernatant. The levels of MDA, SOD, GSH, LDH, and CAT were determined using respective assay kits in accordance with the manufacturer's protocols. ROS levels in HK-2 cells were determined with the ROS kit.

Iron content detection

Renal tissue was homogenized in 0.9% sodium chloride solution at low temperature, centrifuged to obtain the supernatant, and tissue iron content was determined by an assay kit in accordance with the manufacturer's guidelines. Fe^{2+} levels in HK-2 cells were detected with FerroOrange and fluorescence intensity with Image J.

Quantitative real-time PCR (qRT-PCR)

Total RNA was isolated from renal tissue using the OMEGA kit as per the manufacturer's instructions and reverse-transcribed into cDNA with the Roche kit. The mRNA levels of *FN*, *Col1*, *α-SMA*, *CASP3*, *ESR1*, *MTOR*, *NFE2L2*, *PTSG2*, *RELA*, *SRC*, *STAT3*, *TNF*, *and TP53* were assessed by qRT-PCR with SYBR-Green qRT-PCR SuperMix. Gene expression was quantified using the comparative CT ($2^{-\Delta\Delta CT}$) method. Fold changes in experimental samples relative to the control group. Primer sequences are provided in Table 2.

Immunohistochemistry
Fixed renal specimens underwent dehydration via an alcohol gradient, were embedded in paraffin, and sectioned to a thickness of 5 μm. The sections were deparaffinized and dehydrated, followed by a 10-minute incubation with 5% hydrogen peroxide. Antigen retrieval was accomplished by boiling the sections in 1 mol·$L^{[-1}$ sodium citrate. The sections were then blocked with 5% bovine serum albumin (BSA) for 1 h and incubated overnight at 4 °C with primary antibodies against Col1 (1:100), TGF-β1 (1:100), α-SMA (1:100), GPX4 (1:100), NOX1 (1:100), NOX4 (1:100), COX2 (1:100), ACLS4 (1:100), Nrf2 (1:100), and HO-1 (1:100). Subsequently, the sections were incubated with a goat anti-rabbit IgG secondary antibody (1:1000), visualized using HRP-DAB, counterstained with hematoxylin, dehydrated, mounted, and examined under a microscope. Quantitative analysis was carried out using ImageJ software.

Western blotting
Proteins were extracted using RIPA lysis buffer and lysed on ice for 30 min.The supernatant was gathered through centrifugation, and the protein concentration was ascertained with a BCA kit. Proteins were segregated by 12% sodium dodecyl sulfate-polyacrylamide gel electrophoresis (SDS-PAGE), transferred onto a PVDF membrane, and blocked with 1% skim milk for 2 h. Subsequently, membranes were incubated overnight at 4 °C with primary antibodies targeting GAPDH (1:1000), FN (1:1000), Col1 (1:1000), TGF-β1 (1:1000), α-SMA (1:1000), Smad2 (1:1000), p-Smad2 (1:1000), Smad3 (1:1000), p-Smad3 (1:1000), COX2 (1:1000), FTH1 (1:1000), GPX4 (1:1000), Nrf2 (1:1000), and HO-1 (1:1000). Membranes were then incubated with goat anti-rabbit IgG secondary antibody (1:10000), and proteins were visualized using an ECL chemiluminescence kit. Quantitative analysis was performed using ImageJ software.

Collection of DAPA, diabetic RF, and ferroptosis targets
Targets of DAPA were retrieved from the PubChem database (https://pubchem.ncbi.nlm.nih.gov), SwissTargetPrediction database (http://swisstargetprediction.ch/), CTD database (https://ctdbase.org/), and PharmMapper database (http://www.lilab-ecust.cn/pharmmapper/). Targets associated with diabetic RF were identified from the GeneCards database (https://www.genecards.org/) using the search term "diabetic nephropathy and renal fibrosis". The genes related to ferroptosis were obtained from the FerrDbV2 database (http://zhounan.org/ferrdb/current).

Identification of common genes in DAPA, diabetic RF, and ferroptosis
A Venn diagram was constructed using the Omicshare online tool (http://www.omicshare.com/tools) to identify overlapping genes among the three datasets.

Construction of PPI network and identification of core targets
The common target genes were inputted into the STRING database (https://string-db.org/) with 'Homo sapiens' specified as the species and an interaction score threshold set at 0.40. The PPI network was visualized using Cytoscape version 3.10.0, and the top ten genes were identified as core targets based on the MCC score using the cytoHubba plugin.

GO and KEGG pathway enrichment analysis
The shared genes were uploaded to the DAVID database (https://david.ncifcrf.gov/) to conduct KEGG pathway enrichment analysis as well as Gene Ontology (GO) analysis, encompassing Biological Process (BP), Cellular Component (CC), and Molecular Function (MF). A significance threshold was established at a p-value of less than 0.05. Subsequently, the results were exported to Excel, further processed, and visualized utilizing the Omicshare online tool (http://www.omicshare.com/tools) and SRplot (https://www.bioinformatics.com.cn/)[42]. Furthermore, a 'drug-target-pathway-disease' network was constructed via Cytoscape version 3.10.0.

Molecular Docking validation
Molecular docking analyses were executed between the top ten core targets and DAPA using the CB-Dock2 platform (https://cadd.labshare.cn/cbdock2/php/index.php)[43] sourced from the PubChem database and subsequently imported into the CB-Dock2 platform for the addition of hydrogen atoms. The crystal structures of the primary targets were retrieved from the RCSB PDB database (https://www.rcsb.org/), loaded into the CB-Dock2 platform with hydrogen atoms added and all water molecules eliminated. Binding affinity energies were calculated through CB-Dock2 to determine the optimal docking model characterized by the lowest energy.

Statistical analysis
Statistical evaluations were conducted using GraphPad Prism 10.0 software. A one-way ANOVA, complemented by Dunnett's multiple comparison test, was utilized to assess the treatment effects across different groups.

Data availability
Data availability The datasets introduced in this study are accessible in online repositories. All data produced or analyzed during this study can be acquired upon reasonable request to the corresponding author.

Received: 17 November 2024; Accepted: 19 February 2025
Published online: 28 February 2025

References

1. Cole, J. B. & Florez, J. C. Genetics of diabetes mellitus and diabetes complications. *Nat. Rev. Nephrol.* **16**, 377–390. https://doi.org/10.1038/s41581-020-0278-5 (2020).
2. Zhang, K. et al. The role of cellular crosstalk in the progression of diabetic nephropathy. *Front. Endocrinol. (Lausanne).* **14**, 1173933. https://doi.org/10.3389/fendo.2023.1173933 (2023).
3. Gnudi, L., Coward, R. J. M. & Long, D. A. Diabetic nephropathy: Perspective on novel molecular mechanisms. *Trends Endocrinol. Metab.* **27**, 820–830. https://doi.org/10.1016/j.tem.2016.07.002 (2016).
4. Kato, M. & Natarajan, R. Diabetic nephropathy–emerging epigenetic mechanisms. *Nat. Rev. Nephrol.* **10**, 517–530. https://doi.org/10.1038/nrneph.2014.116 (2014).
5. Hung, P. H., Hsu, Y. C., Chen, T. H. & Lin, C. L. Recent advances in diabetic kidney diseases: from kidney injury to kidney fibrosis. *Int. J. Mol. Sci.* **22** https://doi.org/10.3390/ijms222111857 (2021).
6. Yu, X. Y., Sun, Q., Zhang, Y. M., Zou, L. & Zhao, Y. Y. TGF-β/Smad signaling pathway in tubulointerstitial fibrosis. *Front. Pharmacol.* **13**, 860588. https://doi.org/10.3389/fphar.2022.860588 (2022).
7. Meng, X. M., Nikolic-Paterson, D. J. & Lan, H. Y. TGF-β: The master regulator of fibrosis. *Nat. Rev. Nephrol.* **12**, 325–338. https://doi.org/10.1038/nrneph.2016.48 (2016).
8. Park, C. H. & Yoo, T. H. TGF-β inhibitors for therapeutic management of kidney fibrosis. *Pharmaceuticals (Basel).* **15**. https://doi.org/10.3390/ph15121485 (2022).
9. Tian, J. et al. Dapagliflozin alleviates cardiac fibrosis through suppressing EndMT and fibroblast activation via AMPKα/TGF-β/Smad signalling in type 2 diabetic rats. *J. Cell. Mol. Med.* **25**, 7642–7659. https://doi.org/10.1111/jcmm.16601 (2021).
10. Jiang, M., Yang, Z., Lyu, L. & Shi, M. Dapagliflozin attenuates renal fibrosis by suppressing angiotensin II/TGFβ signaling in diabetic mice. *J. Diabetes Complications*. **38**, 108687. https://doi.org/10.1016/j.jdiacomp.2024.108687 (2024).
11. Qiu, X., Bi, Q., Wu, J., Sun, Z. & Wang, W. Role of ferroptosis in fibrosis: From mechanism to potential therapy. *Chin. Med. J. (Engl).* **137**, 806–817. https://doi.org/10.1097/cm9.0000000000002784 (2024).
12. Roccatello, D. et al. From inflammation to renal fibrosis: A one-way road in autoimmunity? *Autoimmun. Rev.* **23**, 103466. https://doi.org/10.1016/j.autrev.2023.103466 (2024).
13. Dixon, S. J. et al. Ferroptosis: An iron-dependent form of nonapoptotic cell death. *Cell* **149**, 1060–1072. https://doi.org/10.1016/j.cell.2012.03.042 (2012).
14. Li, J. et al. Ferroptosis: An important player in the inflammatory response in diabetic nephropathy. *Front. Immunol.* **14**, 1294317. https://doi.org/10.3389/fimmu.2023.1294317 (2023).
15. Chu, J. et al. Advances of Iron and ferroptosis in diabetic kidney disease. *Kidney Int. Rep.* **9**, 1972–1985. https://doi.org/10.1016/j.ekir.2024.04.012 (2024).
16. Heerspink, H. J. L. et al. Dapagliflozin in patients with chronic kidney disease. *N Engl. J. Med.* **383**, 1436–1446. https://doi.org/10.1056/NEJMoa2024816 (2020).
17. Han, L. et al. Structure and mechanism of the SGLT family of glucose transporters. *Nature* **601**, 274–279. https://doi.org/10.1038/s41586-021-04211-w (2022).
18. Huang, Y., Lu, W. & Lu, H. The clinical efficacy and safety of Dapagliflozin in patients with diabetic nephropathy. *Diabetol. Metab. Syndr.* **14**. https://doi.org/10.1186/s13098-022-00815-y (2022).
19. DeFronzo, R. A. SGLT2 inhibitors: cardiorenal metabolic drugs for the ages. *J. Clin. Invest.* **134**. https://doi.org/10.1172/jci177625 (2024).
20. Cai, A. et al. Dapagliflozin alleviates renal inflammation and protects against diabetic kidney diseases, both dependent and independent of blood glucose levels. *Front. Immunol.* **14**, 1205834. https://doi.org/10.3389/fimmu.2023.1205834 (2023).
21. Chen, W. et al. Dapagliflozin alleviates myocardial ischemia/reperfusion injury by reducing ferroptosis via MAPK signaling Inhibition. *Front. Pharmacol.* **14**, 1078205. https://doi.org/10.3389/fphar.2023.1078205 (2023).
22. Wang, Y. H., Chang, D. Y., Zhao, M. H. & Chen, M. Dapagliflozin alleviates diabetic kidney disease via hypoxia inducible factor 1α/Heme Oxygenase 1-Mediated ferroptosis. *Antioxid. Redox Signal.* **40**, 492–509. https://doi.org/10.1089/ars.2022.0169 (2024).
23. Huang, B., Wen, W. & Ye, S. Dapagliflozin ameliorates renal tubular ferroptosis in diabetes via SLC40A1 stabilization. *Oxid. Med. Cell. Longev.* **2022**, 9735555. https://doi.org/10.1155/2022/9735555 (2022).
24. Nogales, C. et al. Network pharmacology: Curing causal mechanisms instead of treating symptoms. *Trends Pharmacol. Sci.* **43**, 136–150. https://doi.org/10.1016/j.tips.2021.11.004 (2022).
25. Sinclair, J. E. et al. Type I diabetes mellitus increases the cardiovascular complications of influenza virus infection. *Front. Cell. Infect. Microbiol.* **11**, 714440. https://doi.org/10.3389/fcimb.2021.714440 (2021).
26. Shu, H. et al. Circular RNAs: An emerging precise weapon for diabetic nephropathy diagnosis and therapy. *Biomed. Pharmacother.* **168**, 115818. https://doi.org/10.1016/j.biopha.2023.115818 (2023).
27. Khalid, M., Petroianu, G. & Adem, A. Advanced glycation end products and diabetes mellitus: Mechanisms and perspectives. *Biomolecules* **12**, (2022). https://doi.org/10.3390/biom12040542
28. Paul, P. et al. Nanomedicines for the management of diabetic nephropathy: present progress and prospects. *Front. Endocrinol. (Lausanne).* **14**, 1236686. https://doi.org/10.3389/fendo.2023.1236686 (2023).
29. Hadpech, S. & Thongboonkerd, V. Epithelial-mesenchymal plasticity in kidney fibrosis. *Genesis* **62**, e23529. https://doi.org/10.1002/dvg.23529 (2024).
30. Wu, Y. & Chen, Y. Research progress on ferroptosis in diabetic kidney disease. *Front. Endocrinol. (Lausanne).* **13**, 945976. https://doi.org/10.3389/fendo.2022.945976 (2022).
31. Li, S. et al. Role of ferroptosis in chronic kidney disease. *Cell. Commun. Signal.* **22** https://doi.org/10.1186/s12964-023-01422-8 (2024).
32. Provenzano, M. et al. Sodium-glucose co-transporter-2 inhibitors and nephroprotection in diabetic patients: More than a challenge. *Front. Med. (Lausanne).* **8**, 654557. https://doi.org/10.3389/fmed.2021.654557 (2021).
33. Scholtes, R. A. et al. The effects of Dapagliflozin on cardio-renal risk factors in patients with type 2 diabetes with or without renin-angiotensin system inhibitor treatment: A post hoc analysis. *Diabetes Obes. Metab.* **22**, 549–556. https://doi.org/10.1111/dom.13923 (2020).
34. Jabbour, S. Durability of response to Dapagliflozin: A review of long-term efficacy and safety. *Curr. Med. Res. Opin.* **33**, 1685–1696. https://doi.org/10.1080/03007995.2017.1354822 (2017).
35. Dharmalingam, M. et al. Evaluating the efficacy, safety, and tolerability of combination therapy of Dapagliflozin and linagliptin over Dapagliflozin and vildagliptin in patients with type 2 diabetes mellitus inadequately controlled with Metformin. *Cureus* **16**, e58115. https://doi.org/10.7759/cureus.58115 (2024).
36. Huang, F. et al. Dapagliflozin attenuates renal tubulointerstitial fibrosis associated with type 1 diabetes by regulating STAT1/TGFβ1 signaling. *Front. Endocrinol. (Lausanne).* **10**, 441. https://doi.org/10.3389/fendo.2019.00441 (2019).
37. Zeng, J. et al. Dapagliflozin alleviates renal fibrosis in a mouse model of adenine-induced renal injury by inhibiting TGF-β1/MAPK mediated mitochondrial damage. *Front. Pharmacol.* **14**, 1095487. https://doi.org/10.3389/fphar.2023.1095487 (2023).
38. Xue, S., Li, Y. X., Lu, X. X. & Tang, W. Dapagliflozin can alleviate renal fibrosis in rats with streptozotocin–induced type 2 diabetes mellitus. *Exp. Ther. Med.* **26**, 572. https://doi.org/10.3892/etm.2023.12271 (2023).
39. Chen, X. et al. Dapagliflozin attenuates myocardial fibrosis by inhibiting the TGF-β1/Smad signaling pathway in a normoglycemic rabbit model of chronic heart failure. *Front. Pharmacol.* **13**, 873108. https://doi.org/10.3389/fphar.2022.873108 (2022).

40. Zeng, X. et al. Mitigation of ROS-triggered endoplasmic reticulum stress by upregulating Nrf2 retards diabetic nephropathy. *Biochem. Biophys. Res. Commun.* **721**, 149972. https://doi.org/10.1016/j.bbrc.2024.149972 (2024).
41. Li, S., Zheng, L., Zhang, J., Liu, X. & Wu, Z. Inhibition of ferroptosis by up-regulating Nrf2 delayed the progression of diabetic nephropathy. *Free Radic Biol. Med.* **162**, 435–449. https://doi.org/10.1016/j.freeradbiomed.2020.10.323 (2021).
42. Tang, D. et al. SRplot: A free online platform for data visualization and graphing. *PLoS One*. **18**, e0294236. https://doi.org/10.1371/journal.pone.0294236 (2023).
43. Liu, Y. & Cao, Y. Protein-ligand blind docking using CB-Dock2. *Methods Mol. Biol.* **2714**, 113–125. https://doi.org/10.1007/978-1-0716-3441-7_6 (2024).

Author contributions

Z.Z.: Writing – original draft, Methodology, Formal analysis, Funding acquisition, Conceptualization. L.L.: Writing – review & editing, Methodology, Investigation, Funding acquisition. Y.D.: Methodology, Investigation, Data curation. Y.L.: Writing – original draft, Methodology, Investigation, Data curation. H.S.: Methodology, Investigation. X.D.: Writing – review & editing, Methodology, Investigation. R.S.: Methodology, Investigation, Data curation. J.Y.: Software, Validation. R.G.: Writing – review & editing, Supervision, Resources, Conceptualization.

Funding

This work was supported by grants from the Postgraduate Research & Practice Innovation Program of Harbin Medical University (No. YJSCX2023-32HYD), Natural Science Foundation of Heilongjiang Province (No. LH2022H099) and Scientific Research Project of Heilongjiang Provincial Health Commission (No. 20240202010154).

Declarations

Competing interests

The authors declare no competing interests.

Additional information

Correspondence and requests for materials should be addressed to L.L. or R.G.